5
Modeling the Spatial Phase Separation Process in Hypermonotectic Alloys

M. Wu, A. Ludwig, L. Ratke

Abstract

A two-phase model is established to simulate the decomposition, macroscopic spatial phase separation due to sedimentation and Marangoni motion, and monotectic reaction in hypermonotectic alloys. Simulations of a 2D square casting with composition (Al-10wt.%Bi) under normal terrestrial and weightless conditions are made. The results for the weightless condition are found to agree qualitatively remarkably well with experiments performed by Walter in sounding rocket experiments using Al-Bi alloys. The results for the normal terrestrial condition agree to a certain extent with experiment performed by Alkemper and Ratke in chill cast Al-Bi alloys. Understanding to the spatial phase separation phenomena in the hypermonotectic alloys is achieved.

5.1
Introduction

Alloys with a miscibility gap in liquid state, especially for those with gross composition beyond the monotectic point (hypermonotectic), are potential bearing materials for automotive industry [1]. A coarse spatial separation of the minority phase from the parent melt seems unavoidable no matter whether the alloy solidifies under normal terrestrial condition [2] or under reduced gravity situation [3–4]. Two mechanisms are responsible for this phenomenon: the gravity induced sedimentation and the Marangoni (thermocapillary) motion. In order to model the phase separation phenomenon, a two phase volume-averaging model, based on the Beckermann's [5–11] and Ludwig's [12–14] previous works on equiaxed solidification, is developed. The ideal spherical morphology of the decomposed second phase droplets permits describing more precisely the growth kinetics of the droplets, their hydrodynamic behavior (drag force), etc. This paper highlights the decomposition of the secondary phase from the parent phase and the spatial phase separation process under normal and under reduced gravity situations.

Solidification and Crystallization. Edited by Dieter M. Herlach
Copyright © 2004 WILEY-VCH Verlag GmbH & Co. KGaA, Weinheim
ISBN: 3-527-31011-8

5.2 Numerical Model

5.2.1 Phase Definition

As shown in Figure 1, at least 4 phases appear in hypermonotectic solidification: the parent melt ($L = L_1$), the secondary liquid phase (L_2), the solidified monotectic matrix (as one phase) and the solidified secondary phase. For simplicity this model considers only two phases: the first liquid phase L_1 and the second liquid phase L_2. During monotectic reaction the monotectic matrix is transformed directly from L_1. Therefore the solidified monotectic matrix is modeled as L_1 phase in such a way that an enlarged viscosity is applied to the L_1 phase on reaching the monotectic temperature. The latent heat of the monotectic reaction is added to L_1 phase. L_2 droplets appearing at the monotectic reaction front are modeled to be entrapped in the monotectic matrix by applying a similar enlarged viscosity at or below the monotectic point. In addition to the above phase definition, following assumptions are made:

(1) Gravity induced sedimentation is modeled with Boussinesq approach;
(2) Both liquid phases have same viscosity;
(3) Eutectic reaction of L_2 is ignored;
(4) No collision and coalescence (coagulation) of droplets;
(5) Diffusion in a single droplet is infinitive, and between droplets is ignored.

5.2.2 Conservation equations

The conservation equations for a two-phase globular equiaxed solidification system have been described previously [12–14]. Modifications are made for hypermonotectic solidification.

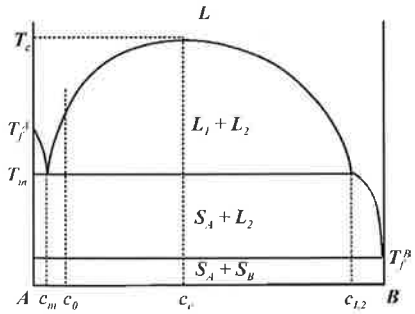

Fig. 1 Schematic phase diagram for systems with a liquid miscibility gap

Mass conservation:

$$\frac{\partial}{\partial t}(f_1\rho_1) + \nabla\cdot\left(f_1\rho_1\vec{u}_1\right) = M_{21}$$
$$\frac{\partial}{\partial t}(f_2\rho_2) + \nabla\cdot\left(f_2\rho_2\vec{u}_2\right) = M_{12} \tag{1}$$

Momentum conservation:

$$\frac{\partial}{\partial t}\left(f_1\rho_1\vec{u}_1\right) + \nabla\cdot\left(f_1\rho_1\vec{u}_1\otimes\vec{u}_1\right) = -f_1\nabla p + \nabla\cdot\bar{\bar{\tau}}_1 + f_1\rho_1\vec{g} + \vec{U}_{21} - \vec{F}_M$$
$$\frac{\partial}{\partial t}\left(f_2\rho_2\vec{u}_2\right) + \nabla\cdot\left(f_2\rho_2\vec{u}_2\otimes\vec{u}_2\right) = -f_2\nabla p + \nabla\cdot\bar{\bar{\tau}}_2 + f_2\rho_2\vec{g} + \vec{U}_{12} - \vec{F}_M \tag{2}$$

where $\bar{\bar{\tau}}_1 = \mu_1 f_1\left(\nabla\cdot\vec{u}_1 + \left(\nabla\cdot\vec{u}_1\right)^T\right)$ and $\bar{\bar{\tau}}_2 = \mu_2 f_2\left(\nabla\cdot\vec{u}_2 + \left(\nabla\cdot\vec{u}_2\right)^T\right)$

The subscripts 1 and 2 in above equations stand for L_1 and L_2 phases. Decomposition, i.e. nucleation and growth (or dissolution) as well as coarsening of the L_2 phase in the parent melt, is taken into account through a mass transfer term M_{12} ($= -M_{21}$). $\vec{F}_M$ is the volume averaged Marangoni force on the L_2 droplets. The enthalpy and species conservation equations are described in literature [12–14].

5.2.3
Droplet Growth and Mass Transfer

A 3-parameter law by Rappaz [12, 15] is employed to model the nucleation of the L_2 droplets. The droplets grow or dissolve by diffusion (Figure 2). The diffusion-controlled growth of a precipitate in a supersaturated matrix was described by Zener [1, 16–17].

$$\frac{dR}{dt} = \frac{D_1}{d_2}\cdot\frac{\Delta c}{\Delta c_d} \tag{3}$$

The radius growth rate dR/dt of a droplet is governed by the difference between the far field concentration c_1 and the interface concentration c_1^* of L_1 phase, i.e. $\Delta c = c_1 - c_1^*$. The solute partitioning at the L_1/L_2 interface is $\Delta c_d = c_2^* - c_1^* \approx c_2 - c_1^*$, where c_2 is the L_2 phase concentration. D_1 is the diffusion coefficient and d_2 is the droplet diameter. When the droplet density n and an additional Avrami-factor f_1 (volume fraction of L_1 phase) are considered, the mass transfer rate M_{12} (kg/m^3/s) is expressed as:

$$M_{12} = n\cdot\pi d_2\cdot\rho_2\cdot\frac{D_1}{c_d}\cdot\Delta c\cdot f_1 \tag{4}$$

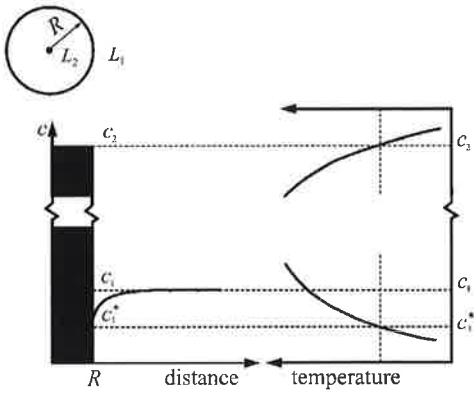

Fig. 2 Schematic of the concentration profile ahead of a growing droplet with respect to the binodal in the phase diagram.

5.2.4
Marangoni Force and Hydrodynamic Resistance

When a droplet is placed in a melt having a temperature gradient, a thermocapillary convection in/around the droplet is induced (Figure 3). The droplet surface is drawn from hotter towards the colder poles in order to lower the surface energy. The consequence is the motion of the droplet towards the hot region. This is called thermocapillary or Marangoni motion. Integration of the thermocapillary force acting on the droplet surface is defined as Marangoni force $\vec{f}_M$ (N). On a droplet having a relative velocity $\Delta\vec{u}$ with respect to the matrix, a hydrodynamic resistance or Stokes force $\vec{f}_{st}$ (N) exists. Based on Stokes-Rybczynski-Hadamard approximation, Young et al [18–20] have deduced $\vec{f}_M$ and $\vec{f}_{st}$ for single droplet.

$$\vec{f}_M = \frac{\pi d_2^2}{(1+\mu_2/\mu_1)\cdot(2+k_2/k_1)}\cdot\frac{\partial\sigma}{\partial T}\cdot\nabla T \tag{5}$$

$$\vec{f}_{st} = 2\pi d_2\cdot\mu_1\cdot\frac{1+3\mu_2/2\mu_1}{1+\mu_2/\mu_1}\cdot\Delta\vec{u} \tag{6}$$

Further considering the droplet density n and the relation $f_2 = n\cdot\pi d^3/6$, the volume averaged Marangoni force $\vec{F}_M$ (N/m^3) in Eq. (2) is expressed as:

$$\vec{F}_M = \frac{6}{(1+\mu_2/\mu_1)\cdot(2+k_2/k_1)}\cdot\frac{f_2}{d_2}\cdot\frac{\partial\sigma}{\partial T}\cdot\nabla T \tag{7}$$

An empirical relationship for the Marangoni coefficient $\partial\sigma/\partial T$ is recommended [1, 17, 21].

$$\frac{\partial\sigma}{\partial T} = -1.26\cdot\sigma_0\cdot\frac{1}{T_c}\cdot\left(1-\frac{T}{T_c}\right)^{0.26} \tag{8}$$

where σ_0 is determined experimentally.

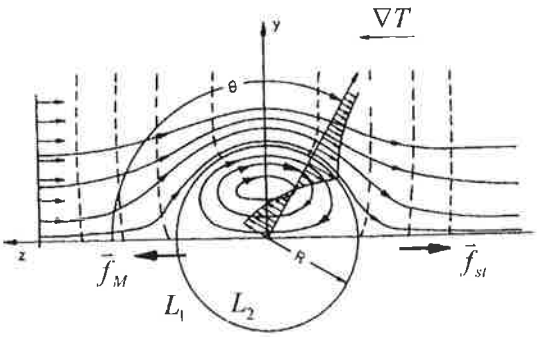

Fig. 3 Thermocapillary convection in and around the droplet.

Momentum exchange $\vec{U}_{12}$ ($= \vec{U}_{21}$) includes two parts: a part due to mass transfer $\vec{U}_{12}^{p}$ and a part due to Stokes force $\vec{U}_{12}^{d}$. Two situations are further considered for $\vec{U}_{12}^{p}$: decomposition (including growth and coarsening) and dissolution respectively. For decomposition, the momentum transferred from L_1 to L_2 is determined according to $\vec{u}_1$, i.e. $\vec{U}_{12}^{p} = \vec{u}_1 \cdot M_{12}$. By analogy we have $\vec{U}_{12}^{p} = \vec{u}_2 \cdot M_{12}$ for dissolution. The Stokes force is expressed as $\vec{U}_{12}^{d} = K_{12} \cdot \Delta\vec{u}$, where K_{12} can be deduced from Eq. (6).

$$K_{12} = \frac{1 + 3\mu_2/2\mu_1}{1 + \mu_2/\mu_1} \cdot \frac{12 f_2}{d_2^2} \cdot \mu_1 \tag{9}$$

Tab. 1 Notation of phase diagram information of Al-Bi system

Monotectic temperature	T_m	930 K	657 °C
Monotectic concentration	c_m	0.47 at. %	3.526 wt. %
L_2 monotectic concentration	c_{L2}	83.4 at. %	97.493 wt. %
Critical temperature	T_c	1310 K	1037 °C
Melting point of Al	T_f^A	933 K	660 °C
Melting point of Bi	T_f^B	543 K	270 °C
Gross concentration	c_0	1.415 at. %	10 wt. %
Slope of liquidus at c_0	m	148.1 K/at.%	20.42 °C/wt.%
Partitioning coefficient	k	51.72	9.55

5.3 Problem description

A 2D square casting (90 × 90 mm^2) with the composition Al-10wt.%Bi is simulated. The mold, remaining at a constant temperature of 290 K, is assumed to be filled instantaneously with melt of initial temperature 1065 K. The heat exchange coefficient at casting-mold interface is 750 W/(m^2.K). The nucleation parameters [15] for L_2 droplets are $n_{max} = 10^{13}$ m^{-3}, $\Delta T_N = 20$ K, $\Delta T_\sigma = 8$ K. Other thermal physical properties and modeling parameters are listed in Table I-II.

Tab. 2 Thermophysical properties used for the simulation [17, 21–22]

ρ = 2340 kg/m	$c_{p(2)}$ = 124.8 J/kg/K	Δh_d = 10.775 kJ/kg
k_1 = 238 W/m/K	$\mu_1 \approx \mu_2 = 1.03 \cdot 10^{-3}$ Kg/m/s	Δh_M = 383 kJ/kg
k_2 = 15.5 W/m/K	$D_1 = 1.1 \cdot 10^{-8}$ m^2/s	σ_0 = 0.1427 J/m^2
$c_{p(1)}$ = 917 J/kg/K	D_2 = 0.0	

5.4 Results and Discussions

5.4.1 Without Gravity

As shown in Figure 4, phase separation, i.e. decomposition and growth with droplet motion is independent of gravity. Marangoni motion presents the only mechanism for the phase transport in the absence of gravity. Droplets of L_2 start to nucleate and grow in the casting surface as the local temperature drops below the binodal (1062.2 K). The Marangoni force causes the L_2 droplets to move from surface regions towards the casting center. The parent melt moves in reverse direction, because the space of the leaving phase L_2 must be replaced by the parent melt L_1. The movement of L_2 will definitely result in depletion of the L_2 phase (f_2) in the corners and surface regions, and enrichment of L_2 phase in the casting center. As the casting further cools down to the monotectic point, monotectic reaction occurs, the velocity of L_1

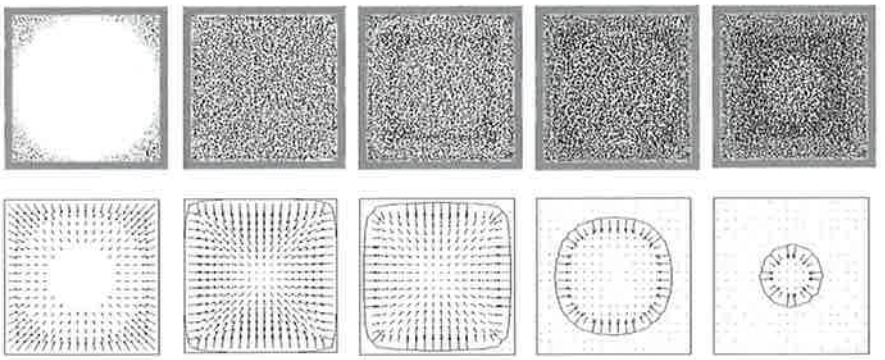

Fig. 4 Solidification sequence without gravity. Top raw: the Bi droplet distribution. The gray matrix means that the alloy has solidified, and the droplets are entrapped in the solid monotectic matrix. Both the droplet density and the diameter of the droplets, shown in this figure, are reduced and enlarged by corresponding factors so that the droplet distribution can be seen with the naked eye. Lower raw: the velocity fields of the second phase droplets together with the monotectic front (T = 925 K).

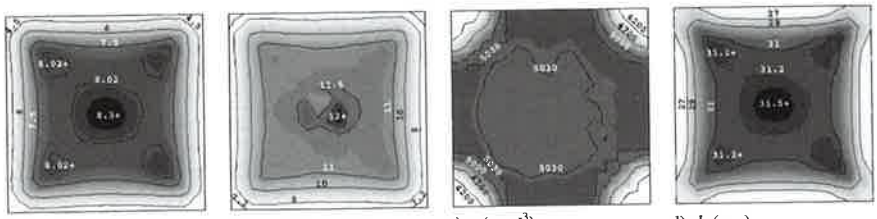

a) f_2 (%) b) c_{mix} (Bi in wt.%) c) n (mm^{-3}) d) d_2 (μm)

Fig. 5 Computer-predicted phase separation, macrosegregation and droplet distribution (without gravity). All quantities are shown with isolines together with 30 gray levels, with dark showing the highest value and bright the lowest.

vanishes and the L_2 droplets are entrapped in the monotectic matrix. When solidification is finished (Figure 5) the surface has a lower volume fraction of L_2 phase ($f_2 <$ 4.5%) and the center has higher volume fraction ($f_2 > 8.3\%$). The spatial separation of the phases is directly responsible for the macrosegregation: $c_{mix} < 7.2\%$Bi in corners, $c_{mix} > 12\%$Bi in center. Both Marangoni motion and diffusion controlled growth contribute to an uneven droplet size distribution. A tendency of finer droplets in the surface regions ($d_2 < 27$ μm) and relatively large droplets in the central region ($d_2 > 31.5$ μm) is predicted. Although the results of Figure 5 have not been experimentally evaluated, the numerically predicted tendency of phase separation agree qualitatively remarkably well with experiments performed by Walter in sounding rocket experiments using Al-Bi alloys [23]

5.4.2
With Gravity

As shown in Figure 6, the droplets of the L_2 phase starts to nucleate in the corners and along the walls, then grow and sink downwards along the vertical walls. As two liquid phases are coupled through the momentum exchange terms the parent melt L_1 phase is drawn by the sinking L_2 phase, forming two vortices: one clockwise in the right half and one anticlockwise in the left half of the casting. The convection currents of L_1 are so strong that they in turn influence the movement and the distribution of L_2 droplets. With the monotectic reaction the L_2 droplets are entrapped in the monotectic matrix, the phase and droplet size distribution remain unchanged afterwards. The final solidification results (Figure 7) show the depletion of L_2 phase in the upper region ($f_2 < 2\%$) and an enrichment of L_2 in the central bottom region ($f_2 > 22\%$ L_2). Strong spatial separation of the phases leads to a strong macrosegregation: $c_{mix} < 5\%$Bi in the upper region, $c_{mix} > 25\%$Bi in the lower bottom region. The droplet distribution pattern is the direct outcome of melt convection and droplet transport. A tendency of small droplets in upper region ($d_s < 18$ μm) and large droplets in the lower bottom region ($d_s > 45$ μm) is predicted. This predicted phase distribution agrees to a certain extent with experiment performed by Alkemper and Ratke in chill cast Al-Bi alloys under terrestrial conditions [24].

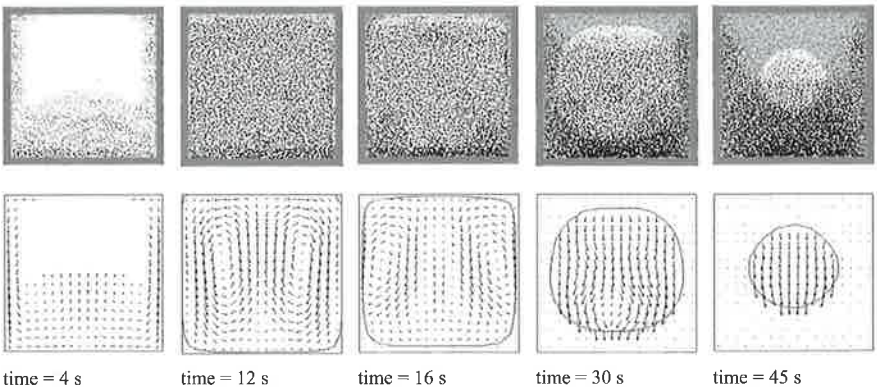

Fig. 6 Solidification sequence with gravity (g = 9.8 m/s^2). Top raw: the Bi droplet distribution. The grey ma trix means that the alloy has solidified, and the droplets are entr apped in the solid monotectic matrix. Both the droplet density and the diameter of the droplets, shown in this figure, are reduced and enlarged by corresponding factors so that the droplet distributi on can be seen with the naked eye. Lower raw: the velocity fields of t he second phase droplets together with the monotectic front (T = 92 5 K).

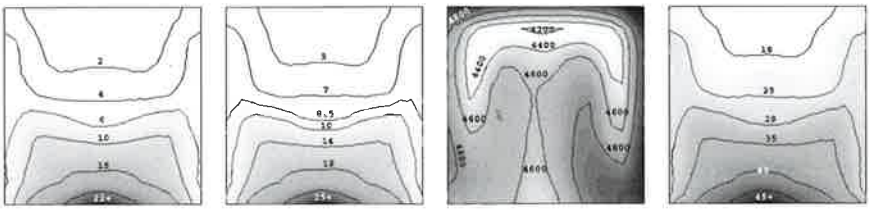

a) f_2 (%) b) c_{mix} (Bi in wt.%) c) n (mm^{-3}) d) d_2 (μm)

Fig. 7 Computer-predicted phase separation, macrosegregation and droplet distribution (g = 9.8 m/s^2). All quantities are shown with isolines together with 30 gray levels, with dark showing the highest value and bright the lowest.

The convection patterns with and without g are totally different. The convection and spatial separation of the two liquid phases with g (max $\vec{u}_2 \approx 81$ mm/s) is much stronger than that without g (max $\vec{u}_2 \approx 0.44$ mm/s). Although both Marangoni motion and gravity induced droplet motion are considered in the case with g, no influence of Marangoni motion on the solidification result is seen. The function of the gravity overwhelms the Marangoni force under normal terrestrial condition as often anticipated in the experimental literature without proof [1–2].

The recent model is established based on some modeling assumptions. For example, the nucleation parameters used in the above simulations were empirically given, and collision and coalescence (coagulation) of droplets are ignored, etc. In order to

evaluate the modeling results, further parameter studies or improvement on the model by releasing some modeling assumptions may be necessary.

5.5 Conclusions

The two phase model described in this paper is able to simulate the decomposition and the spatial phase separation during solidification of hypermonotectic alloys. Nucleation of the secondary phase droplets, droplet growth, Marangoni motion, gravity induced phase sedimentation, parent melt convection, macrosegregation, monotectic reaction, etc. are included. The simulation results demonstrated:

1) Marangoni force under weightless condition causes the L_2 droplets to move from casting boundary regions towards the casting center, and the parent melt L_1 to move in reverse direction, leading to depletion of L_2 phase in the boundary regions and enrichment of L_2 phase in the casting center.
2) Although both gravity induced sedimentation and Marangoni motion occur under normal terrestrial condition, the gravity induced sedimentation dominate the spatial phase separation process. The final results show depletion of L_2 phase in the top region and enrichment of L_2 phase in the middle bottom region.

Collision and coalescence (coagulation) of droplets are not considered in the recent model.

References

[1] L. Ratke, and S. Diefenbach, *Mater. Sci. Eng.*, **1995**, 15(R), 263–347.

[2] B. Prinz, A. Romero, and L. Ratke, *J. Mater. Sci.*, **1995**, 30, 4715–4719.

[3] L. Ratke, G. Korekt, and S. Drees, *Adv. Space Res.*, **1998**, 22, 1227–1236.

[4] L. Ratke, and G. Korekt, *Z. Metallkd.*, **2000**, 91, 919–927.

[5] C. Beckermann, and R. Viskanta, *Appl. Mech. Rev.*, **1993**, 46, 1–27.

[6] J. Ni, and C. Beckermann, *Metall. Trans. B*, **1991**, 22B, 349–361.

[7] C.Y. Wang, and C. Beckermann, *Metall. Mater. Trans. A*, **1996**, 27A, 2754–2764.

[8] C.Y. Wang, and C. Beckermann, *Metall. Mater. Trans. A*, **1996**, 27A, 2765–2783.

[9] C.Y. Wang, and C. Beckermann, *Metall. Mater. Trans. A*, **1996**, 27A, 2784–2795.

[10] C. Beckermann, *JOM*, **1997**, 49, 13–17.

[11] A.V. Reddy, and C. Beckermann, *Metall. Mater. Trans. B*, **1997**, 28B, 479–489.

[12] A. Ludwig and M. Wu, *Met. Trans A.*, **2002**, 33A, 3673

[13] M.. Wu, A. Ludwig, *Adv. Eng. Mater.*, **2003**, 5, 62

[14] M. Wu, A. Ludwig, A. Bührig-Polaczek, M. Fehlbier, and PR. Sahm, *Inter. J. Heat Mass Transfer*, **2003**, 46, 2819–32

[15] M. Rappaz, *Int. Mater. Rev.*, **1989**, 34, 93–123.

[16] C. Zener, *J. Appl. Phys.* **1949**, 20, 950–953.

[17] S. Diefenbach, *Modellierung der*

Gefügeentwicklung von Monotekta, Ph.D. thesis, Ruhr-University Bochum, **1993**.

[18] N. O. Young, J. S. Goldstein, and M. J. Block, *J. Fluid Mech.*, **1959**, 6, 350–356.

[19] W. Günter, *Über die Dynamik von Fluidpartikeln aufgrund des Marangoni-Effektes*, Düsseldorf: VDI-Verlag, **1993**.

[20] M.G. Velarde, in L. Ratke, H. Walter, B. Feuerbacher (Eds.), *Materials and Fluids under Low Gravity*, Springer Berlin, **1995**, 283–298.

[21] F. Falk, in L. Ratke (eds.), *Immiscible Liquid Metals and* Organics, DGM Informationsgesellschaft mbH, **1993**, 93–100.

[22] L. Ratke et al., in L. Ratke, H. Walter, B. Feuerbacher (eds.), *Materials and Fluid under Low Gravity*, Springer Berlin, **1995**, 115–133.

[23] H. U. Walter, in Järva Krog (eds.), *Proc. RIT/ESA/SSC Workshop*, ESA SP 219, Noordwijk, Sweden, **1984**, 47–64

[24] J. Alkemper, L. Ratke, *Z. Metall.*, **1994**, 85, 365–371.